Chapter 4

Synthesis and Characterisation of $La_{2-x}Sr_xNiO_4$

Part of this chapter '**Katheriya, Tarun**, Gurudeo Nirala, and Shail Upadhyay. "Establishing the correlation of negative permittivity and AC conductivity of $La_{2-x}Sr_x NiO_4$ (x= 0, 0.1, 0.3, 1.0) for microwave shielding applications." Journal of Materials Chemistry C 12.23 (2024): 8473-8484'.

4.1 Introduction

Metamaterials are materials that have been created artificially and have some unique properties that are not found in naturally occurring materials. They are composed of periodic arrays of sub-wavelength characteristics and can affect electromagnetic waves in ways that ordinary materials cannot. Such sub-wavelength structures can be tailored to possess certain properties such as a negative refractive index, negative permittivity, or negative permeability by changing their geometry, size, orientation, and composition. In recent years, there has been a lot of interest in left-handed material or metamaterial, which exhibits negative permeability and permittivity in the microwave frequency region. The term "negative dielectric constant" (NDC) refers to phenomena in which the electrical permittivity of a material is negative. Veselago proposed this concept in 1968, stating that it would be possible to create a "left-handed" (LH) material with a negative refractive index using the LH triad formed by the electric field vector, the magnetic field vector, and the phase propagation vector [110].

Due to the complicated nature of meta-materials, researchers tried to explore negative permittivity in composites[14,27,111]. A review article published in 2021 by Kai et. al. highlighted the latest developments in the field of negative permittivity[5]. In this review article, the synthesis and dielectric properties of composites with polymer matrices and ceramic matrices have been described[76,77,112]. The realization of negative permittivity in these composites is observed under specific circumstances, such as the presence of metals in a crucial percolating structure or when their concentration is beyond a particular threshold. After a detailed literature survey on negative permittivity, it has become evident that these composites have certain limitations when applied in situations involving smaller dimensions, such as coatings and thin films. This is primarily due to their non-uniform composition. To address these limitations, researchers have shifted their focus toward exploring materials with

homogeneous compositions, referred to as mono-phase materials. Negative permittivity has been reported in mono-phase materials: Sr-doped $LaMnO_3$[113], Mn-doped Sr_2SnO_4[35], and Nb-doped Sr_2MnO_4[101], Sb-doped SnO_2[95], and Sn-doped In_2O_3[93] at higher temperatures (around 400 °C). We put continuous efforts into achieving negative permittivity at room temperature in pristine (undoped) compounds. We have recently observed negative permittivity at and above room temperature in La_2NiO_4[114].

La_2NiO_4 nickelate with the K_2NiF_4-type structure is an important class of dielectrics that has received increasing attention due to its application as cathode material for Solid oxide fuel cells (SOFCs)[91,115–117]. Previous studies have mostly emphasized the development of La_2NiO_4 as a promising cathode material, there is growing interest among researchers in exploring its dielectric and electrical conductivity properties for other applications. In 2014 Xuan et. al.[118] studied the microwave absorption ability of $La_{1.5}Sr_{0.5}NiO_{4\pm\delta}$ ultrafine particles and reported that an absorption peak of -36.7 dB at a thickness of 3.0 mm covering an absorption bandwidth of 1.4 GHz (9.2–10.6 GHz). Similar behavior of Sr-modified La_2NiO_4 was observed in 2020 [119]. These studies have indicated that the dielectric response and electrical conductivity of La_2NiO_4 can be tailored by the partial substitution of Sr at the La- site. Existing reports reveal that investigations on the dielectric properties of the Sr-modified La_2NiO_4 system have primarily been conducted at low temperatures and at very high frequencies (GHz).

The aforementioned studies have motivated us to conduct a detailed experimental investigation on the structural, micro-structural, electrical properties, dielectric properties, and microwave shielding properties of Sr-doped La_2NiO_4. To achieve the objective, compositions with x = 0, 0.1, 0.3, and 1.0 of the system $La_{2-x}Sr_xNiO_4$ have been synthesized by the solid-state reaction method. Dielectric and electrical properties of synthesized samples have been studied in the Radio-frequency range (20 Hz-2MHz) and temperature range (RT-600^oC) using an LCR meter.

4.2 Sample Preparation

The compositions with x =0, 0.1, 0.3, and 1.0 of $La_{2-x}Sr_xNiO_4$ were synthesized by solid-state reaction method. For convenience, these compositions have been referred to by code name LN0 (x=0.0), LN1 (x=0.1), LaN2 (x=0.3) and LN3 (x=1.0) henceforth. Spectroscopically pure La_2O_3 (Alfa Assar, purity>99.9%) and $NiCO_3 \cdot 2Ni(OH)_2 \cdot xH_2O$ (Sigma Aldrich, purity >99.9%) and $SrCO_3$ (Alfa Assar, purity>99.9%) were taken in a stoichiometric ratio and crushed in a planetary ball mill (Retsch PM 200) in an agate jar and balls (milling vessel is 250ml, and diameter of balls is 10.2 mm) for 15 hrs at 200 rpm taking acetone as a mixing media. During the mixing period ball-to-powder ratio of 5:1 (by weight) was fixed. To prevent the heating and sticking of the powder to the container walls and balls, and agglomeration, the milling sequence was selected such as 15 min of milling followed by 5 min of stop period. The prepared mixtures were dried for a long period (24 hrs) at 80°C in a conventional oven. The calcination of the mixtures was performed at 1200°C (optimized) in a platinum crucible for 12 hrs in an ambient atmosphere. The powders thus obtained were reground with 2% PVA, pressed into cylindrical pellets (10.0 x 2.0 mm), and sintered at 1500°C for 12 hrs with the heating rate of 4° min^{-1} and 2° min^{-1} cooling.

For the microwave shielding measurement, powder of sintered pellets was dispersed in clear epoxy and dried overnight. The weight ratio of Powder/ epoxy for each composite was maintained at 4:1 (each sample contained 80 wt % powder). The samples were cut into the desired rectangular shape, i.e. length a = 23.86 mm and width b = 10.05 mm, and to fit into the wave-guide adapter, with the whole assembly connected to a Vector Network Analyzer (Agilent N5230c, USA) using co-axial cables for microwave property measurements. Full two-port calibration was performed to remove errors. Two coaxial rectangular wave-guide adapters, filling the fixture cross-section, were used to determine the S-parameters and study the

microwave shielding properties of undoped and doped La_2NiO_4 i.e. LN0, and LN2 for comparative study.

4.3 Characterization

The phase purity of the samples was confirmed by recording the X-ray diffraction pattern using CuK_α (λ=1.5406 Å) radiation with the help of a diffractometer (Rikagu X'PERT PRO MPD). The room temperature XRD patterns were collected in the range of 20–80° with a step size of 0.02°. The structure was analyzed by the Rietveld refinement method using the "FullProf program", and a pseudo-Voigt profile function with preferred orientation correction. The microstructure was studied by Bench-top scanning electron microscope (BT-SEM) at room temperature. Valence states of the constituent elements La, Sr, Ni, and O were studied by recording the core spectra of these elements employing an X-ray photoelectron spectrometer (Thermo Fisher Scientific K-Alpha, USA), operating at the high pressure of 5×10^{-11} Torr. The dielectric and electrical properties of samples were investigated using an inductance-capacitance- resistance (LCR) meter (Keysight E-4980A, USA) in a wide range of temperature (40– 600°C) and frequency (20Hz – 2MHz) with a heating rate of 4° min^{-1} in cooling. Silver wires were used as electrodes in the sample holder. Conducting paste was not applied on the surface of the pellets for electrical measurements, as the samples were already conducting. For studying the microwave shielding effectiveness we have used Vector Network Analyzer over two different frequency bands of 1-2 MHz and 8-13 GHz.

4.4 Results and discussion

4.4.1 Phase analysis and crystal structure

It is well known that calcination temperature has a determinant role in the phase purity and morphology of the powders. Mixtures of raw materials were subjected to calcination at 1200

°C for 8 h. Room temperature diffraction pattern of calcined powders was recorded and shown in Figure 4.1(a). The peaks observed in the XRD pattern of the samples have been indexed using the COD *(crystallographic open database)* file of La_2NiO_4. Aside from the La_2NiO_4 peaks, there are a few peaks of very low intensities of raw materials and a peak of secondary phase $LaNiO_3$ was also observed (at 32°). To eliminate the impurity phases and get the desired single-phase materials, pellets of calcined powders were obtained using a stainless-steel die and a hydraulic press.

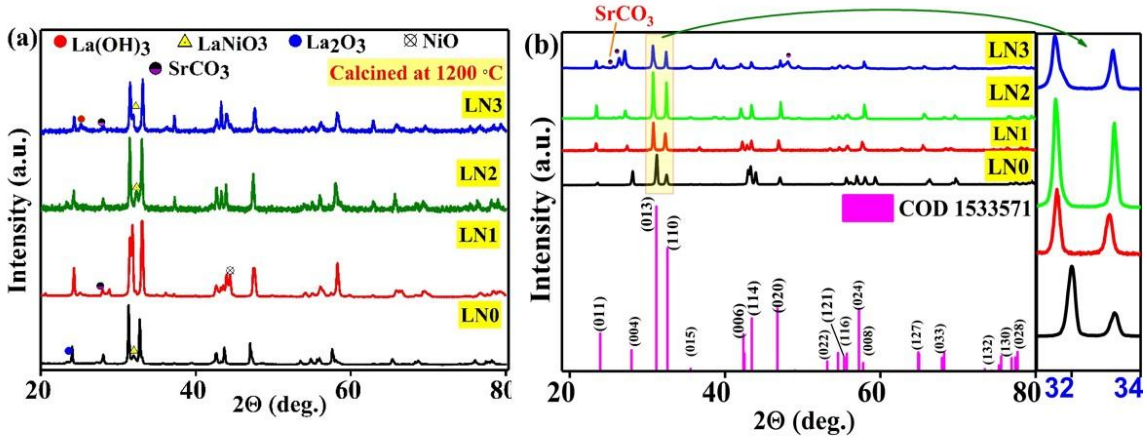

Figure 4.1 X-ray diffraction pattern of (a) calcined powders and (b) sintered pellets.

Pellets made from the calcined powders were sintered at 1500° C for 12 h. Sintered pellets were cleaned and polished and recorded their diffraction pattern is shown in Figure 4.1(b). On matching with the COD file 1533571 (for La_2NiO_4), it was found that peaks of raw materials and secondary phase have now disappeared, and only peaks of La_2NiO_4, except for the composition with x=1.0 (LN3). The disappearance of the unwanted phases at high temperatures may be attributed to the formation of the desired phase as per equation (4.1):

$$LaNiO_3 + xSrO + \frac{1}{2}(1-x)La_2O_3 \rightarrow La_{2-x}Sr_xNiO_4 + \frac{1-x}{2}O_2 \qquad (4.1)$$

In Sample LN3 (x=1.0), Impurity peaks of very low intensity of $SrCO_3$ suggest that the solubility limit of Sr in the lattice of $La_{2-x}Sr_xNiO_4$ solid solution is x<1 in this experiment.

We used the 'Full-Profsuite Programme' to analyze X-ray diffraction patterns using the Rietveld refinement method in order to determine lattice parameters. For comparing the form of diffraction peaks, we used the pseudo-Voigt function. Furthermore, the background is represented by interpolation between collections of background points up to refinable heights. Throughout the process of refinement, important variables were methodically improved. A number of variables have been refined, including lattice dimensions (a, b, c), thermal attributes (B), scale factor, background properties, half-width parameters, zero correction, and positional coordinates (x, y, z) while the occupancy parameters of all ions remained constant during the process of refinement. For the refinement, a tetragonal crystal structure within the space group (I4/mmm) as reported for La_2NiO_4 was adopted. In this structure, La/Sr atoms are situated at the 4e (0, 0, z) sites, oxygen atoms O1 and O2 occupied positions at 4c (0.5, 0, 0) and (0, 0.5, 0), and Ni atoms at the 2a (0, 0, 0) position. The refinement process was in good agreement with the calculated and experimental diffraction patterns as reported previously [120]. The structural parameters obtained after final refinement are presented in Table 4.1.

Table 4.1Parameters obtained from the Rietveld refinement process.

S.N.	Composition	Sample Code	Lattice parameters (Å)	c/a	Volume ($Å^3$)	Density ρ_{exp} (g/cm^3)
1	La_2NiO_4	LN0	a= b= 3.851 c=12.589	3.269	186.697	6.934
2	$La_{1.9}Sr_{0.1}NiO_4$	LN1	a= b= 3.855 c=12.671	3.286	188.304	7.135
3	$La_{1.7}Sr_{0.3}NiO_4$	LN2	a= b= 3.866 c=12.729	3.292	190.247	7.228
4	$LaSrNiO_4$	LN3	a= b= 3.867 c=12.719	3.289	190.196	6.955

From Table 4.1 it is noticed that the lattice parameters increase with increasing doping concentration i.e. x. The linear increase in unit cell volume is also observed. A magnified view of the most intense diffraction peaks (013) and (110) is shown in the inset of Figure 4.1(b). The position of the peaks shifts towards lower angles with increasing doping concentration (x). This shift signifies an expansion of the unit cell. The reason for the expansion of unit cell volume lies in the comparison of atomic radii of dopant Sr^{2+} and host La^{3+} in the same coordination number. The ionic radius of Sr^{2+} is 1.31 Å whereas of La^{3+} is 1.06 Å. Due to the larger atomic

radius of Sr^{2+} in comparison to La^{3+}, the incorporation of Sr^{2+} ions in the lattice of La_2NiO_4 at the La^{3+} ions site leads to an expansion in the unit cell volume. This result becomes evident through the shift of the diffraction peak towards lower angles, as clearly demonstrated in Figure 4.1(b).

In the Perovskite structures, a critical factor influencing crystal symmetry is the tolerance factor, denoted as "***t***". The tolerance factor, a geometrical parameter for A_2BO_4 structures, is defined as follows [35]:

$$\frac{r_A + r_o}{\sqrt{2}(r_B + r_o)} \qquad (4.2)$$

We have calculated the tolerance factor using equation (2.2). In the $La_{2-x}Sr_xNiO_4$ system, the tolerance factor is found within the range of 0.88 (LN0) to 0.97 (LN3), which increases with increasing Sr doping concentration.

4.4.2 Microstructure analysis

The microstructure and surface morphology of sintered pellets were examined using a bench-top scanning electron microscope (BT-SEM). Figures 4.2(a-d) display micrographs of the fractured surfaces at a magnification of 5000x. These micrographs reveal the presence of well-developed, agglomerated grains with cuboidal shapes. The microstructure of La_2NiO_4 (LNO) exhibits some porosity due to its layered structure. Materials of the RP (rock salt and Perovskite) type, have a unit cell structure in which one dimension, responsible for the stacking of Perovskite [ABO_3] and rock salt [A-O] structures, is longer than the other two dimensions. In the lattice of the current RP phase of $La_{2-x}Sr_xNiO_4$, anisotropic thermal expansion is evident, resulting in varying degrees of dilation along different axes, with a more pronounced expansion along the C-axis. This behavior is attributed to the structural diversity of the material.

Consequently, the sintering process, involving thermal cycling, can lead to a combination of grain development and anisotropic modifications, potentially resulting in the formation of micro-pores [84]. From samples LN1-LN3, upon Sr substitution, there is a significant reduction in pore size, leading to improved structural density and denser ceramics. We have calculated the experimental densities of sintered samples at room temperature with the help of a pycnometer (25 ml capacity), using Archimedes' principle. The value of densities for the sample x= 0, 0.1, 0.3, 1 were 89.7% (±0.023%), 91.2% (±0.061%), 93% (±0.049%), and 92.7% (±0.095%) respectively. The density values may initially appear proximate; however, a discernible rise is evident upon the incorporation of Sr doping.

To analyze the grain size distribution in the samples, the ImageJ software package was used. Interestingly, no significant change in grain size was observed. The average grain size, calculated after fitting a Gaussian function to the histograms in Figures 4.2(a-d), is approximately 2 μm.

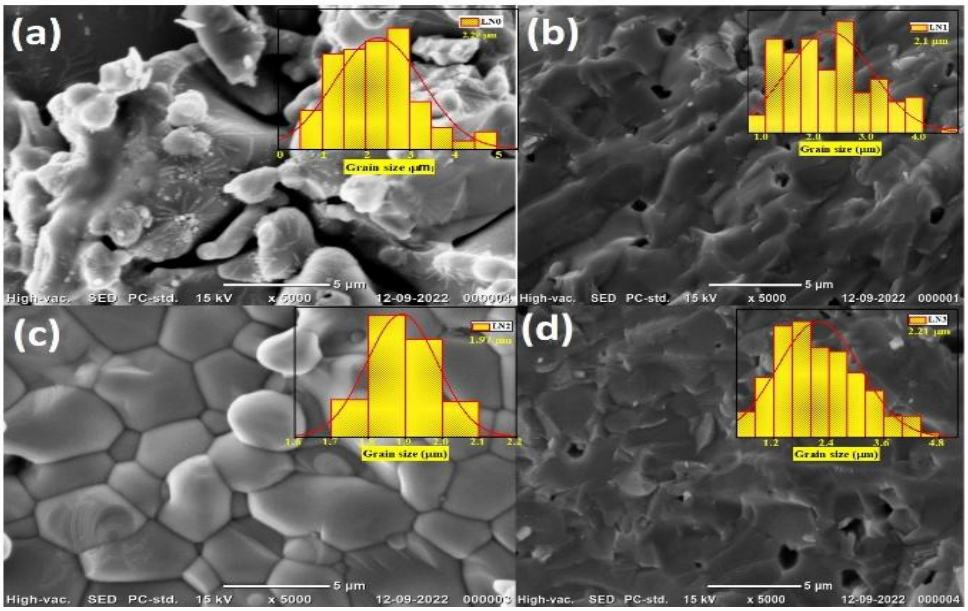

Figure 4.2 SEM images of the fractured surface of the sintered pellets and the histograms showing the distribution of grain size.

4.5 Electrical properties

The variation in the negative permittivity in Sr-doped lanthanum nickelate ($La_{2-x}Sr_xNiO_4$) with changes in temperature and frequency can be understood and explained by doing the analysis of various electrical parameters such as conductivity (σ_{total}), permittivity (ε'_r), conduction- loss (ε_c''), and impedance (Z), along with calculated parameters such as carrier concentration (n_{eff}) and plasma frequency $\boldsymbol{\omega_p}$. We have described these parameters in detail in the following sections.

4.5.1 Negative dielectric constant

The relative permittivity or dielectric constant (ε_r') of the samples was measured over a wide range of temperatures, from 30°C to 600°C, and frequencies ranging from 20 Hz to 2 MHz At 1 kHz frequency variation of relative permittivity with temperature for samples are shown in Figure 4.3 (a). It is observed that the absolute value of the dielectric constant increases with increasing temperature up to a certain temperature, thereafter it starts decreasing for all the samples. The temperature at which trend changes is labeled as transition temperature; it is different for different compositions. In Figure 4.3 (a), we observed that the samples exhibit a plasma-like negative permittivity at all measured temperatures.

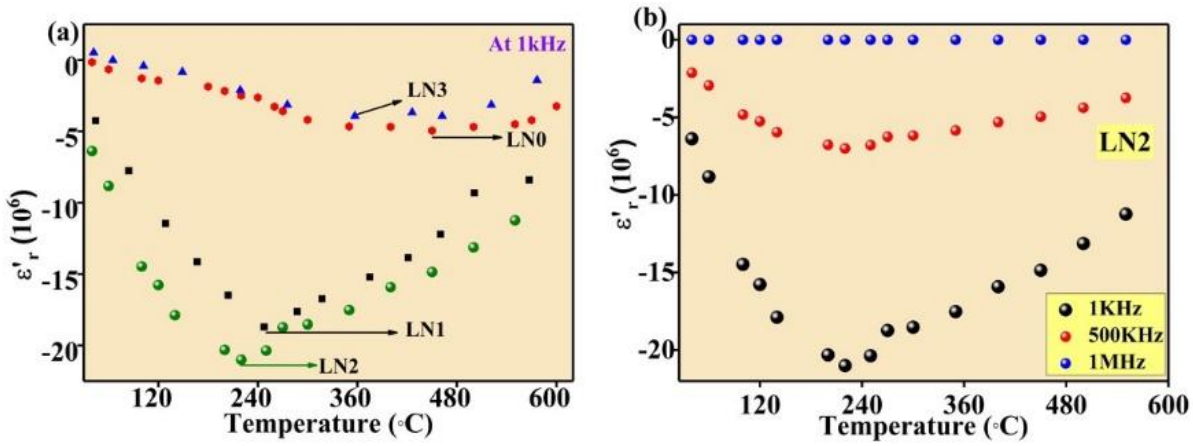

Figure 4.3 Variation of dielectric constant with temperature (a) at 1 KHz (b) at three different frequencies for LN2.

It is observed that with increasing Sr doping concentration (x) transition temperature decreases. For the undoped LNO sample (x= 0), transition temperature was found to be at 450°C. However, in the particular sample LN2 (x=0.3), the transition temperature has dropped substantially to 230°C. On the other hand, magnitude of the dielectric constant increases with increasing doping concentration. These results clearly demonstrate the influence of Sr doping on the dielectric properties of La_2NiO_4. Variations in the dielectric constant of LN2 with temperature, at three different frequencies, are depicted in Figure 4.3(b). The transition temperature remains independent of frequency.

For further investigation into the underlying mechanisms and origin of negative dielectric constant (ε_r') and to explore the influence of doping concentration, we have re-plotted the dielectric constant against frequency at selected temperatures as shown in Figures 4.4(a-c). We can see that as temperature increases, the magnitude of the negative dielectric constant increases up to specific transition temperatures. Beyond these transition temperatures, there is a decrease in its value with further temperature increases. Additionally, as temperature rises, we observe an increase in the dispersion of ε_r' (real part of permittivity) with frequency. This

trend closely resembles previously reported observations, indicating that the temperature-dependent variations in dielectric constant and dispersion are inherent characteristics of the samples and are not attributable to any artefacts stemming from the sample-electrode contribution.

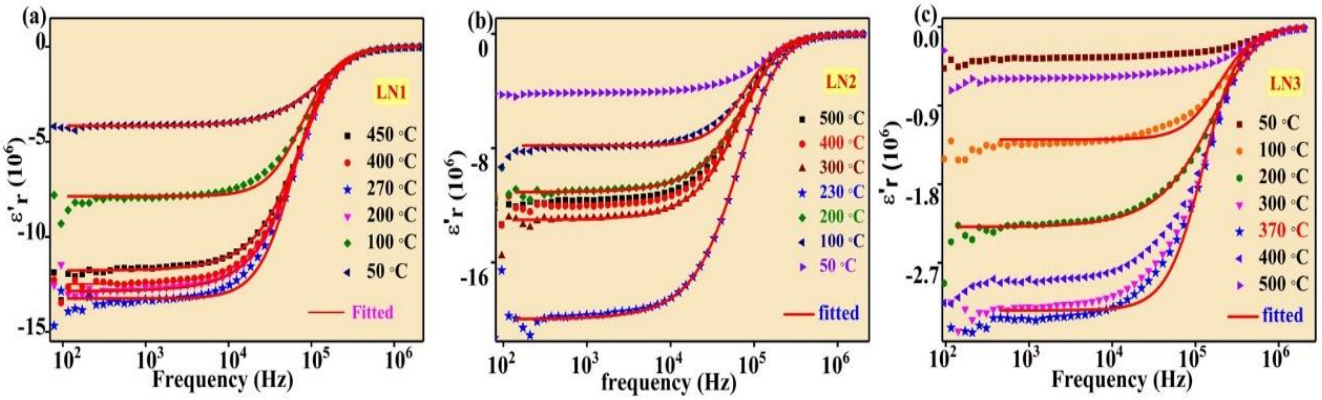

Figure 4.4 (a-c). The variation of real permittivity with frequency at some representative temperature.

In prior studies, two theoretical models, namely the **Drude and Drude-Lorentz** models, have been used to fit the experimental data concerning negative permittivity. Researchers have mostly used the Drude model to elucidate the behavior of negative permittivity in metals and semiconductors [78,121].

According to this model, the real part of the complex permittivity (ε_r') is expressed (4.3):

$$\varepsilon_r' = 1 - \frac{\omega_p^2}{\omega_\tau^2 + \omega^2} \qquad (4.3)$$

In this equation, ω_τ represents the damping factor, which signifies the collision frequency of electrons. On the other hand, ω_p stands for the Drude plasma frequency, and it is correlated to parameters such as carrier concentration (n_{eff}), effective mass (m*), and electronic charge (e) as indicated below:

$$\omega_p = \sqrt{\frac{n_{eff}.e^2}{m^2.\varepsilon_0}} \qquad (4.4)$$

The Drude model (Eqn. (4.3)) was tried to fit the experimental data points shown in Figure 4.4. The solid line represents the data generated by Equation (4.3), while the symbols are the experimental data points. The fitting curves closely align with the experimental data points, indicating a good agreement between the experimental and theoretical data points. This suggests that negative permittivity arises from the ***plasma oscillation*** of free (delocalized) electrons, a phenomenon typically observed in metals and semiconductors. The values of ω_τ and ω_p obtained through the fitting process at various temperatures are given in Table 4.2.

Table 4.2 Parameters obtained from fitting of Drude model to permittivity data.

T (°C)	LN1			LN2			LN3		
	ω_τ (MHz)	ω_P (GHz)	n_{eff} (m^{-3})	ω_τ (MHz)	ω_P (GHz)	n_{eff} (m^{-3})	ω_τ (MHz)	ω_P (GHz)	n_{eff} (m^{-3})
50	1.586	20.36	**~1.72 x 10^{17}**	1.359	23.69	**~1.92 x 10^{17}**	2.601	24.65	**~2.11 x 10^{17}**
100	1.382	20.72		0.940	24.66		2.457	24.4	
150	1.177	21.72		0.796	24.60		2.298	25.11	
200	0.986	21.77		**0.736**	**22.71**		1.870	24.77	
250	0.816	22.15		0.731	22.42		1.664	22.44	
300	**0.803**	**22.35**		0.730	22.37		1.560	22.51	
350	0.851	22.18		0.756	22.21		1.4.95	21.7	
400	0.869	21.07		0.768	22.24		**1.444**	**20.40**	
500	1.002	21.43		0.899	22.14		1.513	26.32	
600	1.072	20.01		1.242	22.65		1.560	26.19	

In the Drude model, ω_τ is related to relaxation time, τ ($\omega = 2\pi f = 2\pi/\tau$) of the charge carriers. In metals, when ω_τ increases with temperature i.e. τ decreases with increasing temperature, it leads to an increase in resistance as temperature rises. However, for synthesized samples ω_τ is decreasing with increasing temperature i.e. τ is increasing with increasing temperature. The

mobility of the electrons is directly proportional to the relaxation time of the electron. The increasing value of τ with temperature indicates an increase in mobility with temperature. In the case of band conduction mobility decreases with increasing temperature whereas in the case of hopping conduction mobility (μ) increases with increasing temperature. Thus, a decreasing value of, ω_τ with increasing temperature suggests hopping-type conduction in the samples.

With the presumption that m* = m, the values of n_{eff} were computed by applying equation (2.4) and are given in Table 2.2. The value of n_{eff} is found to increase slowly as the amount of doping increases. An increase in n_{eff} eventually leads to an increase in conductivity. The dielectric loss (ε_c'') is related to direct current conductivity (σ_{dc}) by the relation $\varepsilon_c'' = \sigma_{dc}/\omega\varepsilon_o$. At room temperature, the variation of ε_c'' against frequency for samples is shown in Figure 4.5. We can see that on increasing Sr concentration, ε_c'' increases.

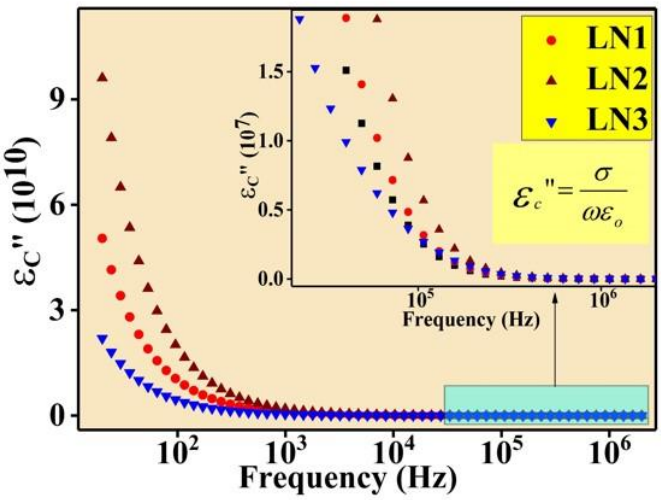

Figure 4.5 Variation of ε_c'' with frequency.

Table 4.3 summarizes the value of ε_c'' at two different frequencies. Values reported in Table 4.3 are approximately 5 orders by magnitude higher than the values reported in the reported literature [122]. ***Cheng. et. al.*** reported strong electromagnetic shielding properties in

carbon/Si_3N_4 due to huge impedance mismatching caused by the high value of negative permittivity and dielectric loss [76]. High values of ε_r' and ε_c'' make these materials suitable for electromagnetic shielding and microwave absorption applications.

Table 4.3 Room temperature values ε_c'' for different compositions at two different frequencies.

Compositions	**1kHz**	**1MHz**
LN1	0.6 $x10^{10}$	2 $x10^{7}$
LN2	11 $x10^{10}$	7 $x10^{7}$
LN3	3 $x10^{10}$	2.1 $x10^{7}$

To confirm the data shown in Table 4.3, we have analysed the same data point in terms of conductivity which is discussed below.

4.5.2 Electrical Conductivity

AC conductivity (σ_{ac}) has been calculated using the measured values of capacitance (c) and dissipation factor (D) in the temperature and frequency ranges that are mentioned above. The relationship between σ_{ac} and frequency at some distinct temperatures is presented in Figure 4.6 (a-c). At low frequencies (up to 100 kHz), σ_{ac} remains constant and independent of frequency. However, at higher frequencies, σ_{ac} diminishes with increasing frequency. This phenomenon is primarily attributed to the ***skin effect*** observed in the conduction of electrons, particularly in metallic materials. The skin effect is a phenomenon that arises at high frequencies, in which alternating current (AC) mostly flows in the outermost layer of a conductor. As the frequency increases, resistance also increases. This happens as a consequence of the AC-inducing self-generated magnetic fields, which lead to an electron concentration close to the surface of the

conductor. Hence, at higher frequencies, electric current flows near the surface of the conductor. This results in to increase in resistance and a decrease in the effective cross-sectional area available for current conduction. The penetration of the current at the surface is known as the ***"skin depth***". The skin depth is inversely proportional to the square root of the frequency and directly proportional to the square root of the resistivity of the material.

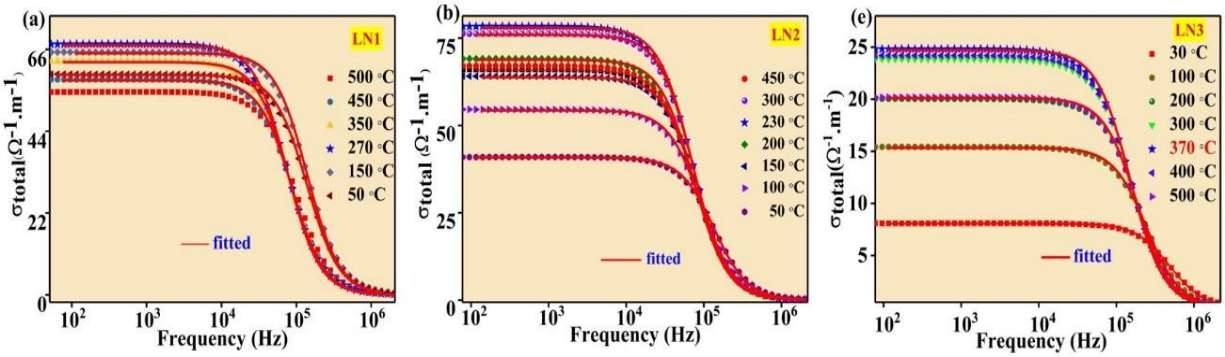

Figure 4.6 Variation of conductivity of samples with frequency at different temperatures.

According to Drude model for AC conductivity of metals[96]:

$$\sigma_{ac} = \sigma_{dc}\frac{\omega_\tau^2}{\omega^2 + \omega_\tau^2} \qquad (4.5)$$

By fitting Equation (4.5) to the experimental points in Figure 4.6, we have determined the values of DC conductivity (σ_{dc}) and ω_τ at different temperatures for all the samples. These results are shown in Table 4.4.

Table 4.4 Fitting parameters obtained from the Drude model for AC conductivity.

Temperature (°C)	**$La_{1.90}Sr_{0.10}NiO_4$ (LN1)**		**$La_{1.70}Sr_{0.30}NiO_4$ (LN2)**		**$LaSrNiO_4$ (LN3)**	
	σ_{dc} (S.m^{-1})	**ω_τ (MHz)**	**σ_{dc} (S.m^{-1})**	**ω_τ (MHz)**	**σ_{dc} (S.m^{-1})**	**ω_τ (MHz)**
100	62	0.837	54	0.98	17	2.54
200	67	0.705	77	0.94	21	2.29
300	66	1.44	75	0.799	24	1.87
400	65	0.869	70	0.760	23	1.74
500	63	1.38	64	0.898	20	1.55

From Table 4.4 it is clear once again, that ω_τ decreases with increasing temperature as it is reported in Table 4.3. DC conductivity increases with increasing temperature up to a particular temperature (transition temperature) and above this temperature, it starts decreasing. Every composition displays an obvious transition in electrical conduction characteristics from ***semiconductor-type to metal-type***, which is similar to previously reported results. The electrical conductivity increases with measuring temperature through a maximum transition temperature and then decreases with the further increment of temperature.

In Figure 4.7, graphs depicting the log of σ_{dc} plotted against 1000/T, shows a linear increase in log σ_{dc} with inverse of temperature show that conductivity. This linear behavior suggests that conductivity obeys Arrhenius relation as given below:

$$\sigma_{dc} = Ae^{-E_a/k_\beta T} \qquad (4.6)$$

where A represents the pre-exponential factor, E_a denotes the activation energy for DC conduction, k_β is the Boltzmann constant, and T denotes the absolute temperature in kelvins (K).

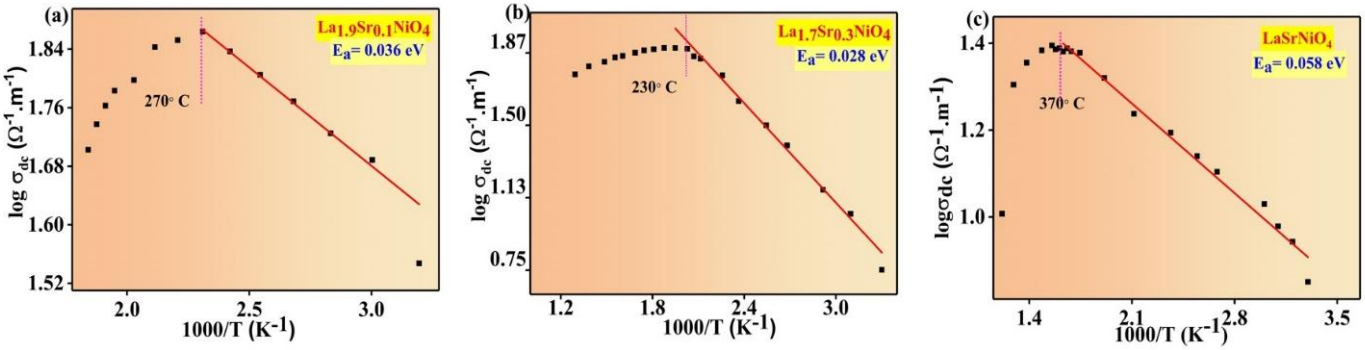

Figure 4.7 Variation of logarithm of DC conductivity with inverse of temperature.

For all compositions, using linear fitting of the measured data (below the transition temperature) value of the slope was computed, and hence the activation energy. The value of the activation energy for all the samples is shown in their respective plot. The value of activation energy, energy needed for the charge carrier to pass through the energy barriers caused by the defects was minimum for sample LN2 and maximum for LN3. The observed value of the activation energy is in agreement with the value reported by other researchers to the "***Small-polaron hopping mechanism"*** in La_2NiO_4 oxide [98,100]. For the composition LN2, we have observed the maximum conductivity of about ~79 Ω^{-1} m^{-1} at 230 °C (transition temperature) which is at least three times higher than the undoped LN0. Similar behavior is observed for other compositions as well at different transition temperatures confirming the intrinsic behavior of Sr doped and undoped layered lanthanum necklets.

According to defect chemistry, the replacement of La by a lower valence element such as Sr would result in either the generation of electron holes at the nickel site or the change in oxygen content [16,22], as described by the below equations:

$$La_{La}^{X} = La_{Sr}' + h^{\bullet} \quad (4.7)$$

$$2La_{La}^{X} = 2La_{Sr}' + V_o^{\bullet} \quad (4.8)$$

$$La_{La}^{X} = La_{Sr}' + Ni_{Ni}^{\bullet} \quad (4.9)$$

It is reported that La_2NiO_4 is a p-type conductor. If charge compensation occurs according to equation (4.7), doping of Sr will generate more charge carriers, and hence conductivity will increase. On the other hand, a decrease in the activation energy with increasing Sr content is possible due to an increase in the number of hopping sites. An increase in the hopping sites may be possible on partial oxidation of Ni^{2+} to Ni^{3+} oxidation.

To reveal the valance state of individual elements, present in the samples and support the above explanation, we have performed an XPS analysis.

4.6 XPS analysis

To reveal valence states for the constituent elements (La, Ni, Sr, and O) in $La_{2-x}Sr_xNiO_4$, X-ray photoelectron spectroscopy (XPS) was used. The survey scan data for La_2NiO_4 is presented in Figure 4.8(a), revealing particular peaks corresponding to the elements La (3d), Ni (2p), Sr (3d), and O (1s). To establish binding energies, the C1s peak at 285 eV was employed as a reference. Core level spectra for Ni 2p, La 3d, Sr 3d, and O (1s) are depicted in Figure 8 (b-e). These core level peaks were fitted using the Shirley function.

In Figure 4.8(b), the XPS spectra of Ni for various compositions reveal two distinct peaks at 855.2 eV and 851.6 eV. These peaks can be attributed to the characteristic peaks of Ni $2P_{3/2}$ and the satellite peak, respectively. This observation suggests that the chemical state of Nickel is predominantly Ni^{2+} in the LN0, in agreement with previous reports [34]. However, for LN1 and LN2, the presence of Ni^{3+} is confirmed, as indicated by the presence of two peaks around 872 eV, corresponding to Ni^{3+} states [90,91].

The XPS spectra of La 3d for LN0, LN1, and LN2 are presented in Figure 4.8 (c) and primarily exhibit the spin-orbit splitting of La $3d_{5/2}$ and $3d_{3/2}$, as previously reported [34]. In the synthesized samples, the characteristic peaks of $3d_{5/2}$ are centered at 834.28 eV and 838.29 eV, while the peaks of $3d_{3/2}$ are located around 851.53 eV and 855.14 eV. These findings strongly suggest that Lanthanum in all the samples predominantly in the La^{3+} state.

Core shell XPS spectrum of Sr 3d is shown is Figure 4.8 (d) and mainly consist of the spin-orbit splitting of Sr 3d into Sr $3d_{5/2}$ and Sr $3d_{3/2}$ respectively. For both the samples LN1 and LN2, the representative peaks of Sr $3d_{5/2}$ are around 133 eV, and for Sr $3d_{3/2}$ are around 134 eV respectively confirming the valance state of Sr is +2 in both the samples [123].

Conversely, in the XPS spectra of the O (1s) spectrum depicted in Figure 4.8 (e), a single peak is discerned, which can be further deconvoluted into three distinct peaks. These peaks have been attributed to different oxygen species. The lower binding energy peak, located at approximately 528.3 eV, corresponds to OH^- adsorption whereas peak at 531 eV belongs to lattice oxygen. The increase in the intensity of OH^- on increasing the concentration of Sr at 528 eV is because Sr^{2+} is more prone to OH^- adsorption than La^{3+} and hence equation (2.7) could be the possible mechanism describing the charge compensation responsible for the partial

oxidation of Ni^{+2} into Ni^{+3}, It is also observed that peak assigned to lattice oxygen is becoming symmetric towards higher binding energy is an indication of decrease in the oxygen vacancies.

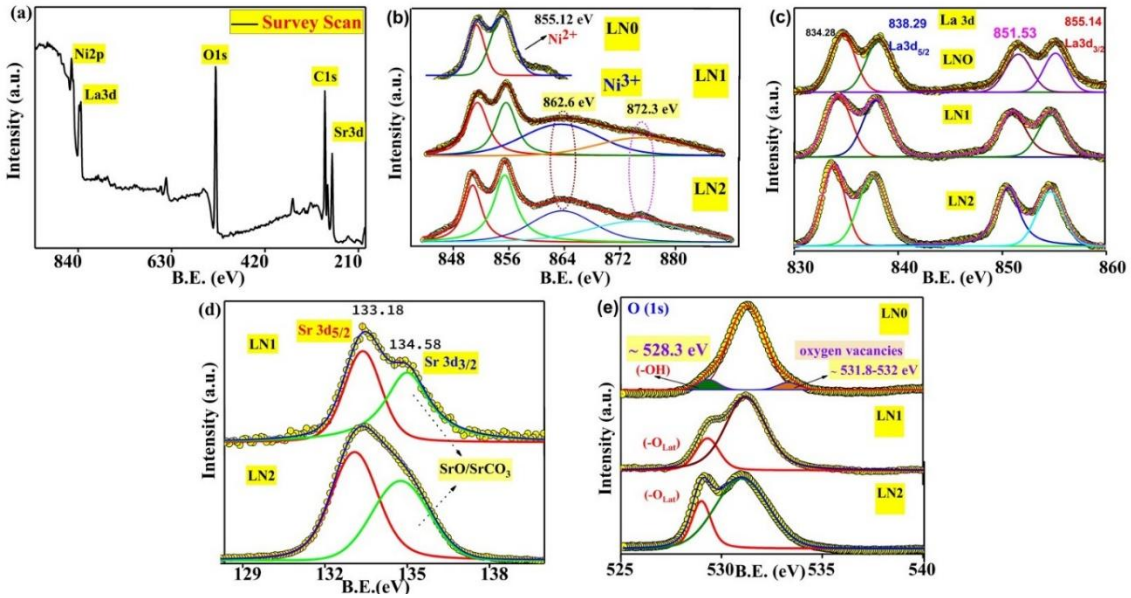

Figure 4.8 The XPS spectrum (a) Survey scan (b-e) core level of Ni, La, Sr, and O.

4.7 Impedance analysis

The "reactance" is a key parameter that helps us understand the phase relationships between current and voltage when an alternating electric field is applied. On the basis of the sign of reactant, we can differentiate capacitor and inductor. When voltage lags behind the current, we observe a negative reactance, indicating the capacitive nature of the material. Conversely, a positive reactance suggests inductive characteristics, where the current phase lags behind the voltage phase. This subtle polarity in reactance holds significance for comprehending and utilizing material electrical properties, making it relevant in various research and technological applications [102,104–107].

There was a corresponding relation between permittivity and reactance:

$$\varepsilon' = -\frac{Z''}{2\Pi f C_o\left[\left(Z'^2\right) + \left(Z''^2\right)\right]} \quad (4.10)$$

Where, Z' is resistance, Z'' is reactance, C_0 is the vacuum capacitance, and f is test frequency.

Figure 4.9 (a) shows the frequency dependences of reactance for samples with different amounts of Sr-dopant at room temperature. The reactance displayed an escalating trend with the increase in frequency. For $La_{2-x}Sr_xNiO_4$ ceramics (where x varies from 0 to 1), it was observed that the reactance remained consistently positive across the entire range of test frequencies. Furthermore, the corresponding real permittivity exhibited a negative value, attributed to the occurrence of plasmonic oscillations. A similar behavior was observed by many researchers [79].

Meanwhile, Figure 4.9 (b) gives the frequency dependence of impedance phase angle for samples with different Sr-dopants. The positive phase angle suggests that the phase relationship between voltage and current in epsilon-negative samples is absolutely different from that in positive permittivity materials. With Sr- dopant increasing, the ceramics exhibit a higher phase angle.

As indicated in Figure 4.9 (C), the variation of Z'' with Z' also confirms that the reactance is positive. The Z' value at the lowest frequency (represented by the intercept on the x-axis) decreases as the Sr concentration increases. It is important to clarify that Z' signifies DC resistance, and this decrease in value with rising Sr concentration suggests that the samples are exhibiting a more pronounced inductive behavior. In other words, the inductive characteristic was responsible for negative permittivity from the perspective of impedance property [95].

Here, it's important to note that the possibility of stray inductance provided by the sample holder and its connecting wires may unwittingly contributed to the experimentally observed impedance values. Since the total measured impedance, values are small in magnitude. Therefore, it is necessary to take this into account and separate the unintentional contribution caused by the sample holder's impedance from experimentally collected data before analyzing the reactance behavior of synthesized samples.

For this purpose, different combinations of resistors and inductors were tried to model and simulate the experimentally measured impedance data using Z-view simulation software. For sample LN2 equivalent circuit as shown in the inset of Figure 4.9 (d) is found to be the most suitable circuit to represent the experimentally measured impedance data. Further, the obtained results were validated through complex fitting in Origin Pro17. In Figure 4.9 (d) the values of R1, R2, L1, and L2 were obtained from complex impedance data fitting of the equivalent circuit. Figure 4.9 (e-f) is the simulated version of the same data using z-View software.

For other samples, similar processes were used and the findings are summarized in Table 4.5. It is observed that values of R1 and L1 are very small compared to R2 and L2. Therefore we have assigned R1 and L1 to the contribution from the wires and sample holder and R2 and L2 is the contributions from our samples

Table 4.5 Values obtained from complex fitting the impedance data for various compositions.

Sample	R1(m Ω)	L1 (μH)	R2 (Ω)	L2 (H)
LN1	4.23	10	191	62
LN2	4.17	11	120	87
LN3	4.11	11	147	23

Negative dielectric behavior is caused by plasmonic oscillations of free charge carriers. The plasmonic oscillation of these charge carriers in an applied sinusoidal electric field gives rise to surface current. The origination of the sample's inductive behavior (L2) can be attributed to this current on the surface of the sample. The resistance (R2) can be attributed to the resistance offered to this circulating current on the grains' surface and/or resistance offered to the conduction current within/through the grains.

Furthermore, our materials with negative permittivity offer significant inductance similar to conventional wire-wound inductors. Therefore, exploring negative permittivity materials holds great research potential for developing coil-less electric inductors [50].

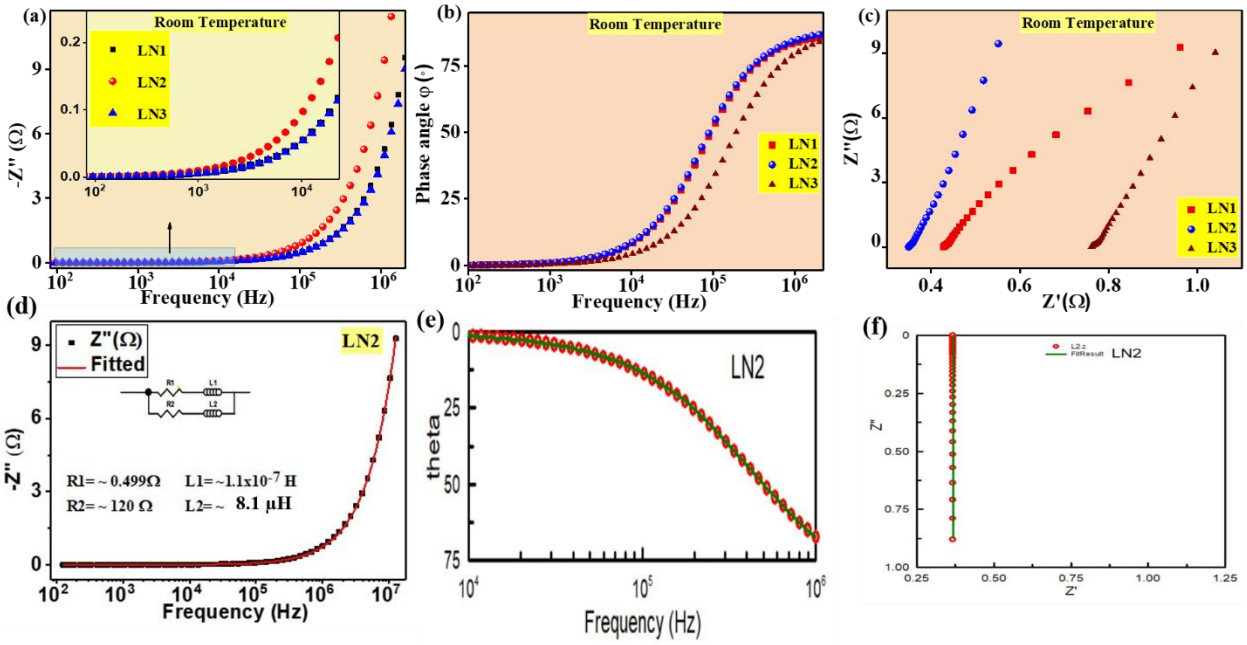

Figure 4.9 The room temperature variation of (a) reactance (z"). (b) Phase angle. With frequency (c) Z" vs Z'. (d-f) corresponding fitting of the experimental data.

4.8 EMI Shielding Effectiveness Studies

The effectiveness of Electromagnetic interference (EMI) shielding relies on three primary mechanisms: reflection, absorption, and multiple internal reflection [6]. EMI shields primarily reflect radiation, utilizing charge carriers that interact with EM fields, thus requiring high electrical conductivity. Absorption of EM radiation, facilitated by interactions with electric/magnetic dipoles, electrons, and phonons, along with properties like thickness, and electrical permittivity. Multiple internal reflections within the material significantly contribute to EMI shielding effectiveness, stemming from scattering centers, interfaces, or defect sites, resulting in multiple scattering and EM wave absorption. The total shielding effectiveness (SE_T) includes shielding due to reflection (SE_R) arising from an impedance mismatch between air and the shielding material while shielding due to absorption (SE_A) dissipates electromagnetic microwaves in the shield. The absorption of EM energy (SE_M) correlates with multiple internal reflections.

Total shielding effectiveness (SE_T) would be given by [124]:

$$SE_T = SE_A + SE_R + SE_M \quad (4.11)$$

where SEA and SER are evaluated from the scattering parameters (S11 and S21) obtained using a two-port vector network analyzer [125–128].

We have explicitly calculated the reflection loss (SEr) and absorption loss (SEa) using the measured S-parameters, based on the following relations:

$R = |S_{11}|^2$, $T = |S_{21}|^2$, $A = 1 - R - T$, $SE = -10\log_{10}(T)$, $SE_R = -10\log_{10}(1 - R)$

When the total shielding effectiveness of the material is more than 10 dB, then loss due to multiple reflections (SE_M) becomes negligible and can be neglected [42].

Thus, the total shielding effectiveness (SE_T) now can be expressed as

$$SE_T = SE_A + SE_R \quad (4.12)$$

where SE_A and SE_R can be directly calculated by the S-parameters obtained from the two-port VNA measurement [125–128].

$$SE_A = 10\log\left(\frac{T}{1-R}\right) \quad (4.13)$$

$$SE_R = 10\log\left(1-R\right) \quad (4.14)$$

In linear form, the reflection coefficient is $R=|S_{11}|^2$, the transmission coefficient $T = |S_{21}|^2$, and the absorption coefficient is $A=1-R-T$.

Figure 4.10(a) represents the material under test. Figure 4.10(b-d) illustrates the variation of different microwave shielding parameters SE_R, SE_A, and SE_T in the frequency range of 8–13 GHz. Figure 4.10(b), represents that reflection phenomena dominate the shielding mechanism. The total shielding effectiveness (SE_T) is approximately ~15 dB for sample LN0 and, about ~47 dB for sample LN2 i.e. (**99.99% total transmission reduction/attenuation**) at 8.54 GHz with a matching thickness of only 2 mm, which is higher than previously reported data [119]. This increase in SE_T is attributed to the higher conductivity of LN2 compared to LN0, resulting from the presence of plasmons (delocalized electrons).

Similarly, to provide an inclusive understanding of its shielding effectiveness at lower frequencies as well, Figure 4.11 further examines their Total Shielding Effectiveness in the 1-2 MHz region. SE_T for sample LN0 is about ~11 dB to ~15 dB and for LN2 is between ~41 to ~45 dB. These frequency ranges are crucial for assessing the effectiveness of the shield in practical electromagnetic interference shield developments.

It is important to mention that the desired EMI shielding effectiveness for commercial applications is approximately 20 dB, which corresponds to equal to or less than 1% transmittance of electromagnetic waves. Hence, there is an expectation that our improved material could be more suitable for various commercial applications.

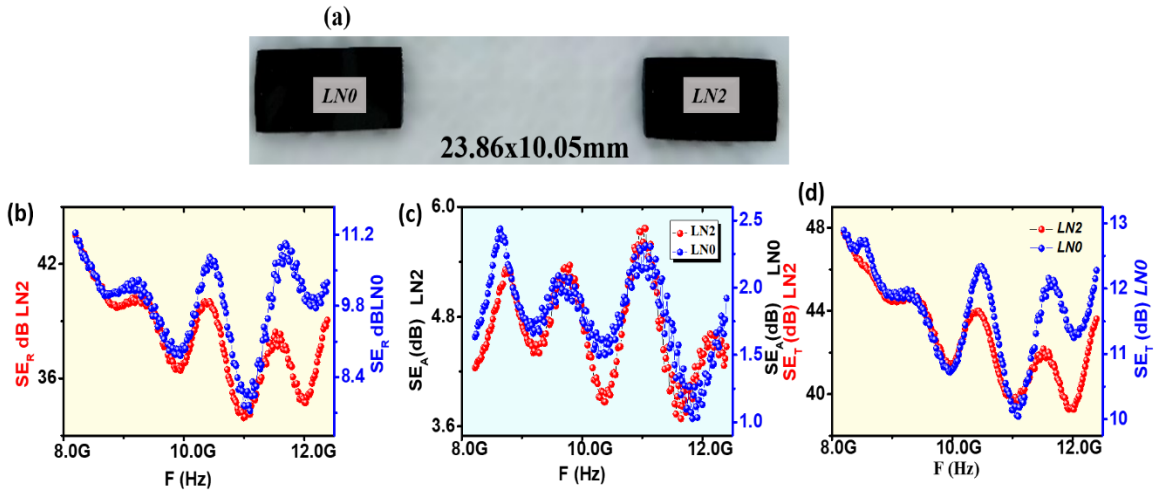

Figure 4.10 (a) Schematic diagram of samples for the measurement. Variation of shielding effectiveness parameters (b) reflection (SE_R), (c) absorption (SE_A), and (d) total (SE_T) with frequency.

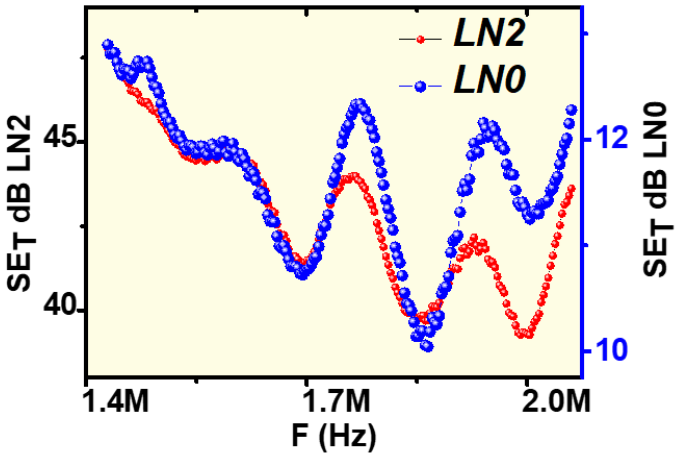

Figure 4.11 Variation of total shielding effectiveness (SE_T) with frequency.

4.9 Conclusion

In this paper, we have tried to establish the correlation between electrical conductivity, and negative dielectric constant. Single-phase Sr-doped La_2NiO_4 was successfully synthesized using the solid-state reaction method. Examination of the SEM image verified the irregular growth of cuboidal-shaped grains. The real part of permittivity consistently exhibited negative

values across all tested frequencies and temperatures. The experimental data points were well-fitted by the Drude model, and this negative permittivity behavior was attributed to the plasma oscillation of free charge carriers. The lower activation energy (E_a) for DC conduction indicated a small polaron hopping conduction mechanism. Positive values of the imaginary part of impedance (Z'') confirmed inductive behavior across the entire range of temperature and frequency measurements. The microwave studies indicate a prominent rise in total shielding effectiveness (SE_T) upon the incorporation of Sr (LN2) compared to the undoped sample (LN0).

It can be inferred from the observations that a higher magnitude of electrical conductivity leads to a larger negative permittivity, which in turn causes a stronger impedance mismatch. This results in an increase in the Total Shielding Effectiveness (SE_T) value of the samples. This outcome signifies the potential to tune and modify the microwave shielding properties by compositional modification for a variety of applications.